Check for updates

Received: 2 July 2022 | Revised: 22 November 2022 | Accepted: 21 January 2023

DOI: 10.1111/jace.19020

Journal of the American Ceramic Society

RESEARCH ARTICLE

Actinide and lanthanide dioxide lattice dilatation mechanisms with defect ingrowths

Seçkin D. Günay

Department of Physics, Faculty of Science, Yıldız Technical University, Esenler, Turkey

Correspondence
Seçkin D. Günay, Department of Physics, Faculty of Science, Yıldız Technical University, Esenler, 34210, İstanbul, Turkey.
Email: sgunay@yildiz.edu.tr

Abstract

The effects of irradiation-induced defects on the fluorite-structured dioxide materials were investigated in the literature and explained with complex physical phenomena. An interpretation that can simply explain their effects on the structure has not been put forward so far. However, in a recent atomistic simulation study, a specific defect was found to be directly responsible for the α-particle irradiated UO_2 lattice dilatation, and there was a linear relationship between them. It was also determined that this linear equation has two different slopes at low and high defect concentrations. In this paper, it was found that these phenomenon were not specific to UO_2 and applicable to all fluorite-structured actinide and lanthanide dioxides studied here (CmO_2, AmO_2, CeO_2, UO_2, NpO_2, PuO_2, ThO_2). The findings provide clues to the existence of more general law. The results have the potential to lead to significant improvements, such as why different radiation types (α-particle, α-decay, fission) swell the lattice at different saturation levels.

KEYWORDS

actinide dioxide, alpha-particle, defect, lanthanide dioxide, lattice dilatation, swelling

1 | INTRODUCTION

Studies on irradiated materials have been performed for decades. Part of these studies has been done on various actinide and lanthanide oxides.[1–22] The importance of some of these materials stems from their use in the nuclear energy industry. Different levels of radiation doses and types have diverse effects on these materials—various levels of formation of defects, amorphization, swelling, change in mechanical, and thermal properties, etc. These can affect the entire energy production process and an in-depth study of radiation-induced events at the atomic level is necessary to understand the complex mechanisms. The existence of a simple approach that explains the fundamental mechanism of all could make significant contributions to nuclear power technology and beyond. In this study, the problem will be addressed at an elementary level by examining single-crystal systems with isolated defects. For this reason, much attention would be paid to swelling of single-crystals due to α-particles, where α-particles have a weak radiation effect, can displace a few atoms, and transfer little energy to the crystal. The results to be obtained will help to explain the complex situations that occur with other types and high-energy radiations toward the end of the study.

In this study, lattice dilatation mechanisms and defect ingrowth of some single-crystal fluorite-type isostructural oxides (actinide and lanthanide dioxides, i.e., CmO_2, AmO_2, CeO_2, UO_2, NpO_2, PuO_2, ThO_2) due to α-particles were examined by classical molecular dynamics simulation method. Results were compared with available experimental and molecular dynamics (MD) simulation results.[1–6] The effect of irradiation on the crystal was modeled by two techniques: "manual defect creation" (MDC) method[7,8] and a widely used "displacement cascade" (DC) method. In our previous study,[7] as a result of the calcu-

 © 2023 The American Ceramic Society.

lations made with the first method, the obstruction type (OT) defect was directly responsible for the change in the UO_2 lattice parameter. There was a linear relationship between the number of OT uranium defects and the relative lattice expansion of UO_2. Moreover, an increase in the slope of the linear equation was observed above a critical number of OT uranium defects. In this study, the existence of a similar relationship will be questioned for other isostructural dioxides (CmO_2, AmO_2, CeO_2, NpO_2, PuO_2, ThO_2), and how these defects change the physical properties of molecules. The sensitivity of obtained results for UO_2[7] on input parameters was examined by changing the interaction potential, the irradiation method, the number of atoms in the simulation box, and the MD simulation program. In addition to these studies, the amount of lattice dilatation of some actinide dioxide materials (CmO_2, AmO_2, PuO_2, UO_2) caused by self irradiation as a result of α-decay[1,9–19] and other radiation type[20] was compared with the obtained data. Although no comparisons had been made with other self-irradiated actinide dioxides ((U, Th)O_2, MOX),[21,22] discussions were also performed on these molecules.

To briefly clarify the terminology used in the article, the OT cation is a defect enclosed in an octahedron structure and surrounded by six other cations. It can be easily seen from the ⟨110⟩ direction and got this name because it obstructs this channel. All OTs in this study are Frenkel defects, as they leave their original position and settles in an interstitial site.

2 | METHODS

In this study, a pair potential with the many-body embedded atom model was used to model the interactions between ions.

$$E_i = \frac{1}{2}\sum_j \phi_{\alpha\beta}\left(r_{ij}\right) - G_\alpha\sqrt{\sum_j \sigma_\beta\left(r_{ij}\right)}$$

The first part is the pair-wise interaction term, and the second part is the many-body term. The pair-wise term consists of parts such as long-range Coulomb, Morse, and Buckingham interactions. The cut-off distance was determined as 11.0 Å for short-range interaction potentials. Potential parameters for some isostructural oxides (CmO_2, AmO_2, CeO_2, UO_2, NpO_2, PuO_2, ThO_2) were tabulated by Cooper et al.[23] They were utilized in the LAMMPS program.[24]

Two methods were used to model the irradiated crystal. The first method is the "manual defect creation" method used by the author of this article in his previous works.[7,8] The second is the frequently used "DC" method. Besides being a more realistic method, the second method was applied to dispel doubts about the validity of the first method.

2.1 | First method: Manual defect creation

Molecular dynamics simulation supercell boxes (10 × 10 × 10) were constructed for oxide molecules. α-irradiation damage was modeled by randomly moving cations in the crystal structure. They were relocated manually from their normal position to interstitial sites, which are called initial Frenkel pairs (IFPs). The simulation was re-initialized each time a new cation IFP defect was introduced in the simulation box. Thus, the number of defects was increased one by one to reach the maximum value of 140 IFP. This was determined by considering the point at which the swelling of the crystal reached saturation.

Each IFP cycle starts by moving a cation. Since this artificial positioning of cations adds a large amount of energy to the structure, the simulation was initiated by an energy minimization technique. The steepest descent algorithm was used for energy minimization. Subsequently, supercells with 0 bar pressure were annealed for 100 ps at 300K temperature. Constant pressure and constant temperature ensemble (NPT) ensemble was applied to the simulation box, which allows the change of three axes independently. The system was exposed to a heat bath by a so-called Nose-Hoover thermostat to keep the temperature constant. Relaxation times are 0.5 ps for the barostat and 0.1 ps for the thermostat. Lattice constants, atomic coordinates, radial distribution functions, etc., were saved to calculate physical properties like the number of defects, interatomic distances, and swelling.

In experiments conducted with α-particle radiation,[1–3] α-particles acting on one side of the structure affect the entire crystal equally. Based on these experiments, all cations were shifted in the Y-Z layer to model homogeneous irradiation from one side of the crystal.[7,8] Defects were not placed in the successive layers to prevent instant annihilations. At some point, for a high number of IFPs, the artificially created defects were so close to each other that it became difficult to maintain this limitation.

2.2 | Second method: DC

Another method for modeling alpha particle radiation is to create energetic particles in the MD simulation box. Our aim here is to create an environment similar to experimental conditions. This simulation method is widely used to study irradiated crystals. In the experiments car-

15512916, 2023, 6, Downloaded from https://ceramics.onlinelibrary.wiley.com/doi/10.1111/jace.19020 by Yildiz Teknik University, Wiley Online Library on [10/07/2025]. See the Terms and Conditions (https://onlinelibrary.wiley.com/terms-and-conditions) on Wiley Online Library for rules of use; OA articles are governed by the applicable Creative Commons License

ried out by groups,[1–4] the oxide crystals were exposed to mono-energetic ∼ 5.5 MeV α-particle radiation. Physical properties were observed while increasing the radiation dose. Our simulation model, which was built on these foundations, was initiated with an energetic atom. The high-energy atom is called primary knock-on atom (PKA) and gains its energy by the impact of an α-particle. Initial velocity was assigned to create the high-energy initial state of the PKA atom. The PKA transferred this energy to other atoms in the crystal, and a DC would occur within the simulation box.

Embedded-atom method (EAM) model was used for interactions between atoms. Ziegler-Biersack-Littmark (ZBL) screened Coulomb potential was applied to avoid non-physical situations in interactions between atoms that occur at very small distances during the collisions of high-energy particles. EAM potential was splined to ZBL potential by following the steps in a previous study.[25] MO_2 (M = Cm, Am, Ce, U, Np, Pu, Th) simulation boxes of 20 × 20 × 20 size were created with fluorite structure. In the first step, MD simulation was initiated by applying energy minimization (steepest descent algorithm) to the crystal structure. In the second step, the perfect crystal structure was equilibrated with an NPT ensemble for 10 000 steps with 0.5 ps barostat and 0.1 ps thermostat relaxation times. The dimensions of the MD box were allowed to move independently. The crystal structure was exposed to 300K temperature and 0 bar pressure. The time step in this part of the simulation is 1fs. In the third step, after the minimization and the equilibration steps, the DC process was launched. The ensemble utilized to the simulation box had been changed to microcanonical ensemble (NVE). Velocity rescaling thermostat was applied to the outer layer of the simulation box, ∼ 2Å thick in the Y and Z directions, thereby removing the extra energy transferred by the PKA to the MD simulation box. Since the initial velocity of the cation (PKA) was selected in the X-direction, a velocity rescaling thermostat had not been performed in a slab in the X-direction to reduce the interaction of PKA with the thermostat. As a result, this thermostat was applied to plates covering four sides of the box. Randomly selected PKA were given energy of 100 eV (see Supplementary Material-1). All of the PKAs were selected from cations. The initial velocities of these atoms were chosen in the X-direction since the irradiation was made from one side of the crystal surface.[1,3] The variable time-step algorithm had been applied, which is used in DC simulations where forces are very large. Thus, the computation time was minimized. The time step was allowed to change between $10^{-5} ps$ and $10^{-3} ps$. This part was carried out for 50 000 steps. In the fourth part, the box was exposed to an NPT ensemble with similar conditions above (second part) for 20 000 steps to observe and collect results of the irradiation event. The third and fourth steps (radiation cycle) were repeated many times in succession to complete the entire alpha-particle irradiation process. The alpha-particle dose is gradually increased in the experiments, similarly, the PKA number was incremented by one at the beginning of each "radiation cycle" in the simulation. For example, in the first radiation cycle, one PKA, in the second radiation cycle two PKAs, etc., were created in the box. These cycles were repeated until the swelling reached a saturation point, which occurs between 140 and 200 for all oxides and 100 eV PKA energy. This value will be called the "PKA number.". In both methods mentioned above (MDC and DC), the reason for increasing the "PKA number" and the "cation IFP" one by one is to correlate with the increase of the α-particle dose in the experiments.

3 | RESULTS

Fission and α-particle irradiation effects and thermal recovery of uranium dioxide were investigated by the author of this article in previous studies.[7,8] In this study, calculations were further expanded by investigating the effects of α-particles on isostructural oxides. Numerous experiments have been conducted on fluorite-structured compounds, which were exposed to α-particle irradiation, He ion implantation, Ce irradiation or α-decay events. Damage ingrowth, swelling, formation of defects, lattice recovery and damage annealing were mainly investigated in some actinide dioxides, that is, CeO_2,[3] CmO_2,[10,11] AmO_2,[12–15] PuO_2,[3,12,16–19] UO_2,[1–3,5,6,20] $(U,Th)O_2$,[21] MOX.[22] The calculated results will be compared with these data.

3.1 | Lattice parameter

3.1.1 | Saturation points

Artificial defects called IFPs were created by the random displacement of cations in the simulation box with the first method (MDC). The data corresponding to each cation IFP are independent simulations of 100 ps in Figure 1. There are 140 data points for each oxide. The variation of fractional changes in lattice parameters $(\Delta a/a_0) \times 10^4$ with the IFP displayed exponential changes for all isostructural oxides.

The variation of the fractional changes in lattice parameters to the "PKA number" is shown in Figure 2 by using the second method (DC). Detailed information about the meaning of the horizontal x-axis, which is the "PKA number," is explained in the methods section. A smooth and vibration-free exponential increase is observed between 0 and 60 PKA numbers for all oxides. Above this point, the

15512916, 2023, 6, Downloaded from https://ceramics.onlinelibrary.wiley.com/doi/10.1111/jace.19020 by Yildiz Teknik University, Wiley Online Library on [10/07/2025]. See the Terms and Conditions (https://onlinelibrary.wiley.com/terms-and-conditions) on Wiley Online Library for rules of use; OA articles are governed by the applicable Creative Commons License

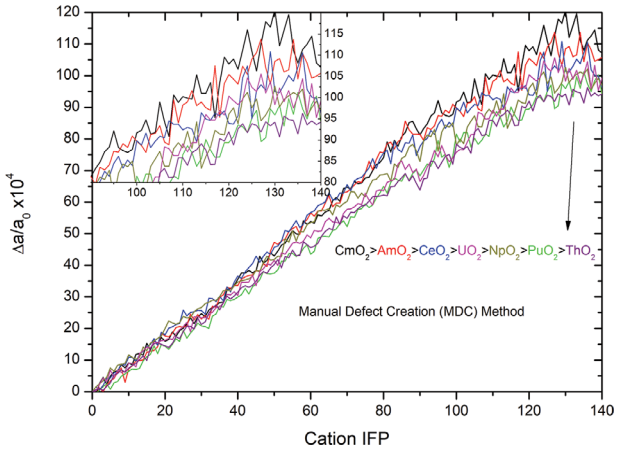


FIGURE 1 The variation of changes in lattice parameters with the cation IFP (initial number of Frenkel pairs) using manual defect creation (MDC) method.

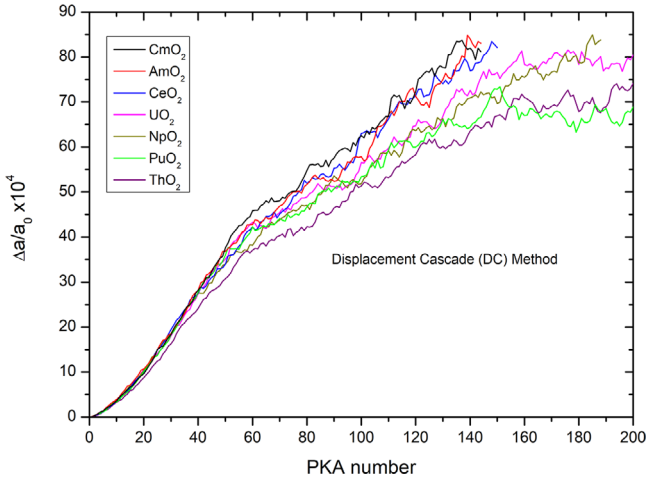


FIGURE 2 The variation of changes in lattice parameters with the PKA (primary knock-on atom) number using displacement cascade (DC) method.

behavior of the exponential curve changes, the vibrations gradually increase, the slope of the curve slowly decreases and eventually reaches the saturation point. Due to the excessive deterioration in crystal structures and the increase in defect clusters at high PKA number, some of the simulation cells have become unable to maintain their cubic structures and abrupt elongation occur in those cubic structures. For this reason, data above that point where the corruption of the crystal occurred was ignored and excluded from the graph. It is seen that molecules other than UO_2, ThO_2, and PuO_2 are affected by this situation. Interestingly, the 0.82%–0.84% range on the y-axis seems to be an upper bound for all oxides, above which large-scale disruption is observed regardless of the molecule type. As can be seen in Figure 2, more data cannot be obtained from the calculations for CmO_2, AmO_2, CeO_2, and NpO_2 molecules above this point.

The saturation points of single and polycrystalline structures calculated by experimental and classical MD simulation methods are listed in Table 1. Simulation results of single-crystal oxide structures in the second and third columns were acquired from Figures 1 and 2, and compared with Weber's experiments[3] on α-particle irradiated polycrystalline materials in the fifth column. Δa and a_0 are the change in the unit cell size and the lattice constant of the perfect crystal, respectively. Although the second and third columns are the single-crystal, and the fifth column is the polycrystalline structure, results show that there is a correlation between both data groups, and a decrease is observed from top to bottom. A similar study[7] previously conducted on the $8 \times 8 \times 8$ single-crystal UO_2 supercell with a different interaction potential[26,27] in another MD program[28] using the MDC method yielded ~1.05%, which is very close to the results attained in the current study (~1.03%) with the same method. In 2016, Chartier et al.[6] performed simulations with Frenkel pairs accumulation (FPA) method to simulate ballistic damages in single-crystal UO_2. The saturation point value they found was ~1.3% (see Table 1). Data are close to the value we found with the MDC method. The results obtained with both MD methods (MDC and FPA) overestimates the experimental value (α-particle irradiation with PuO_2 source),[1] because MD studies are designed to transfer a small amount of energy to the system. However, they are compatible with 20-keV He ion irradiation experimental result (~1%)[5] in Table 1 that transfers little energy to the system.

As a result, the calculations made with MDC and DC method show that the saturation points (Table 1) for oxides from large to small values can be listed as follows: CmO_2, AmO_2, CeO_2, UO_2, NpO_2, PuO_2, ThO_2. Even though the saturation points of the four molecules (CmO_2, AmO_2, CeO_2, NpO_2) were not revealed by the DC method, the general behavior of the curves along the entire figure (Figure 2) confirms this order. Consequently, our calculations resemble the experimental results, which were the fractional change in lattice parameters as a function of α-particle radiation doses of polycrystalline fluorite-structured actinide dioxides.[3]

The amount of swelling in the single-crystal material is higher than in the polycrystalline material. Experimental saturation point data are 0.84% and 0.58% for single-crystal[1] and polycrystalline[3] UO_2, respectively (Table 1). Single-crystal data are about 45% higher than polycrystalline data. Since there are no experiments of α-particle irradiation effects on the single-crystal structures of other oxides in the literature, simple inferences can be made about what results would be achieved if α-particle irradiation experiments were performed on these

15512916, 2023, 6, Downloaded from https://ceramics.onlinelibrary.wiley.com/doi/10.1111/jace.19020 by Yildiz Teknik University, Wiley Online Library on [10/07/2025]. See the Terms and Conditions (https://onlinelibrary.wiley.com/terms-and-conditions) on Wiley Online Library for rules of use; OA articles are governed by the applicable Creative Commons License

TABLE 1 The saturation point values of change in lattice parameters, $(\Delta a/a_0)\%$, were listed. The second and third columns were MD results of single-crystal structures from this study. MD (Frenkel pairs accumulation method) result of another group was given in the fourth column. In the fifth and the sixth column, α-particle damage experimental data of single and polycrystalline oxides were given. Data[5] in the sixth column are from the 20-keV He ion implantation experiment. In the seventh and eighth columns, self-radiation damage experiments due to α-decay (α-particle and α-recoil atom bombardment) on single and polycrystalline oxides were listed. (Dist.: The simulation cell gets distorted before reaching saturation point.)

Molecule	(MD, Single-Crys)—Method 1 (MDC)	(MD, Single-Crys)—Method 2 (DC)	(MD, Single-Crys)—(FPA Method)	(Exp, Poly-Crys, α-Irr)	(Exp, Single-Crys, α-Irr)	(Exp, Poly-Crys, Self-Rad)	(Exp, Single-Crys, Self-Rad)
CmO_2	~1.14%	Dist.	–	–	–	0.3%[10]0.233%[11]	–
AmO_2	~1.09%	Dist.	–	–	–	0.338%[12]0.239%[13]0.2	–
CeO_2	~1.05%	Dist.	–	0.73%[3]	–	–	–
UO_2	~1.03%	0.76%−0.81%	~1.3%[6]	0.58%[3]	0.84%1%[5]	–	0.4%−0.5%[1]
NpO_2	~1.00%	Dist.	–	–	–	–	–
PuO_2	~0.98%	0.63%−0.73%	–	0.46%[3]	–	0.338%[12]0.283%[16]0.3	–
ThO_2	~0.94%	0.67%−0.73%	–	–	–	–	–
$(U, Th)O_2$	–	–	–	–	–	–	~0.5%[21]
MOX	–	–	–	–	–	0.29%[22]	–

Abbreviations: DC, displacement cascade; MDC, manual defect creation; FPA, Frenkel pairs accumulation.

single-crystal structures, assuming similar relationships between single and polycrystalline structures as in UO_2. Saturation points of α-particle irradiated single-crystals could be found roughly by using saturation point values of α-irradiated polycrystalline isostructural oxides (CeO_2, PuO_2) in Table 1. However, it should be noted that this is only an assumption. Finally, it is seen that the saturation point (0.76%−0.81%) of the single-crystal UO_2 structure found by the DC method is also compatible with the single-crystal experimental data (0.84%). DC method appears to be a suitable and realistic method for modeling a structure exposed to alpha-particle radiation.

3.1.2 | Dependence on the radiation type

Experiments show that the saturation level of the lattice parameter expansion, $(\Delta a/a_0)\%$, varies depending on the type of radiation. The saturation levels of single-crystal UO_2 in descending order are α-particles (~0.8%), α-recoil (0.4%−0.5%), and fission (~0.1%).[1,21] Primary atomic displacements per interacting particle were listed as, 100 for α-particle irradiation, 1500 for α-decay, and 100000 for fission events.[21] The main reason for the difference between saturation points is the probability of creation and annihilation of these instantaneous defects.[2,16] As it is understood from the previous discussions,[21] it was commented that the α-particles have lower removal rates of defects from the lattice by recombination, annihilation, or clustering than other radiation types. In some studies,[1,4] it had been mentioned that thermal spikes of fission and α-recoil events contributed to the recombination or the cluster formation of defects. It was concluded that defect annealing and clustering took place along the track of α-recoil atoms.

The data obtained from our previous studies[7,8] provide information about the defects responsible for the irradiation-induced swelling in uranium dioxide crystal lattice structures. It was concluded that the amount of lattice dilatation depends on the number of OT defects. These defects are uranium and oxygen ions for α-particle radiation and fission events, respectively. Their structures and surrounding atoms were revealed.[7,8] The saturation level of lattice expansion for α-recoil-damaged uranium dioxide structure is between α-particle and fission damage saturation levels.[1] It could be concluded that thermal spikes play a critical role in the difference among the saturation levels of these three events and lead to a significant change in the amount of OT cation defects. In the fission event, based on the previous findings,[7] it could be estimated uranium atoms are displaced from their normal positions to form OT uranium defects, but almost immediately these defects annihilate or recombine as a result of thermal spikes. Thus, a limited amount of swelling occurs with OT oxygen defects remaining in the lattice.[7] The saturation level in the α-recoil event demonstrates that the OT uranium defects are partially recombined as a result of thermal spikes. The thermal effect is not sufficient to eliminate all of them, or the effect is limited to certain regions where thermal

15512916, 2023, 6, Downloaded from https://ceramics.onlinelibrary.wiley.com/doi/10.1111/jace.19020 by Yildiz Teknik University, Wiley Online Library on [10/07/2025]. See the Terms and Conditions (https://onlinelibrary.wiley.com/terms-and-conditions) on Wiley Online Library for rules of use; OA articles are governed by the applicable Creative Commons License

spikes take place. The recombination of defects as a result of thermal spikes and the formation of defects as a result of radiation come about simultaneously, and an intermediate saturation level for α-recoil event take place higher than the fission event and lower than α-particle radiation. This creates an uncertainty and randomness in the level of saturation point.

Self-irradiation from α-decay, that exhibits both α-particle irradiation and the α-recoil event, data on actinide oxides (CmO_2, AmO_2, UO_2, PuO_2, (U, Th)O_2, MOX) in the literature are listed in Table 1. Experimental saturation point data display various values are not consistent among themselves. For example, as shown in Table 1, saturation points of fractional lattice parameters for PuO_2 are between 0.283% and 0.39%, and for AmO_2 are between 0.239% and 0.35%. Therefore, the relationships found in columns two, three, and five do not exist in column seven, and no comparison can be made. Main reason for this, as discussed above, is thermal spikes caused by α-recoil atoms and the resulting random annihilation of cation defects. Data from our previous studies[7,8] demonstrated the importance of the effect of cation Frenkel (OT) defect pairs. The uncertainty in the number of thermal spikes and the amount of temperature increase in the crystal makes it challenging to predict the number of remaining OT cation defect pairs and the corresponding swelling. Besides all these, the dilation in lattice constants is sensitive to the preparation conditions of samples.[21] Therefore, there is no relationship between our data and the experimenters' data. Thermal spikes also occur in the case of α-particle radiation, but this takes place in a limited number and intensity. This weak effect eliminates a small amount of OT defect and slightly reduces the increase in lattice constant. In another experiment with 500 keV Ce irradiation applied to the single-crystal UO_2 structure,[20] the saturation point was obtained around ~0.53%, close to the α-decay result. It appears that not all OT defects survive and some are eliminated for the reasons listed above.

3.1.3 | Effects of OT cation defects on lattice parameters

The formation of OT cation defects as a result of α-particle irradiation has a primary effect on the dilation of the crystal. As observed in the previous study,[7] there is a linear relationship between the number of OT uranium defects and lattice swelling. This interesting result remained valid even if the number of atoms in the simulation (supercells with $5 \times 5 \times 5$ and $8 \times 8 \times 8$ unit cells) or the interaction potential (was tested with two different potentials) had been changed.[7] Again in this study, the number of atoms in the simulation box was increased to $10 \times 10 \times 10$ and $20 \times 20 \times 20$. A new interaction potential was employed. Another MD program was used. In addition to the previous irradiation method (MDC), a new one had been applied (DC). Thus, the sensitivity of the previously obtained data to simulation inputs (atom number, interaction potential, irradiation technique, MD program) was tested for uranium dioxide. The presence of a similar linear behavior in other oxides was also investigated here using the similar inputs.

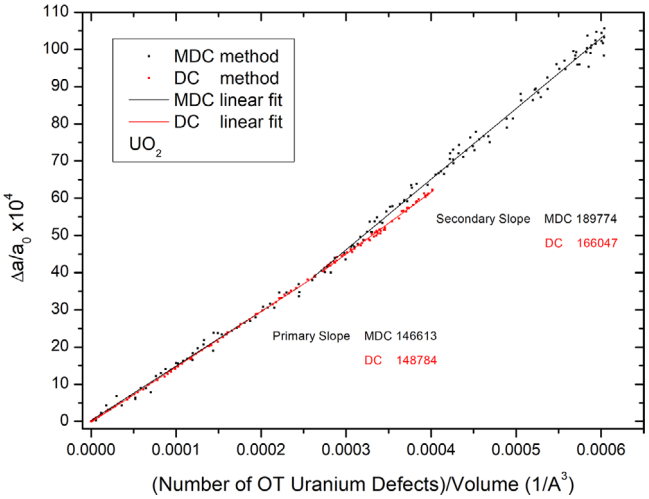


FIGURE 3 The lattice parameter changes of UO_2 versus the obstruction type (OT) uranium defect concentration using manual defect creation (MDC) and displacement cascade (DC) methods. Linear curve fitting was applied to the data.

Uranium dioxide

In this study, the swelling of oxides by radiation was modeled using two different methods. Each method was applied to simulation boxes containing various numbers of atoms ($10 \times 10 \times 10$ and $20 \times 20 \times 20$ for MDC and DC methods, respectively. The size of the simulation boxes were adjusted according to the method.). Unlike our previous studies,[7,8] to compare the simulation boxes with different numbers of atoms, the x-axis of the graph (Figure 3) will be plotted as the defect concentration instead of the defect number. Similar to our previous studies, despite the changes in input parameters mentioned above, linearity still exists between OT uranium defect concentration (the number of OT uranium defects/volume) and the fractional change in the UO_2 lattice parameter in Figure 3. The lattice parameter change ascended with the increase in OT uranium defect concentration, and the linear relationship was maintained up to 0.36%−0.39%. The gradient of the graph changed above this point, resulting in another linear equation with a steeper slope value. The secondary linear equation ended up around a maximum of ~1.04% for the MDC method and ~0.62% for the DC method. Recipe used

15512916, 2023, 6, Downloaded from https://ceramics.onlinelibrary.wiley.com/doi/10.1111/jace.19020 by Yildiz Teknik University, Wiley Online Library on [10/07/2025]. See the Terms and Conditions (https://onlinelibrary.wiley.com/terms-and-conditions) on Wiley Online Library for rules of use; OA articles are governed by the applicable Creative Commons License

to calculate the number of OT defects was clearly stated in our previous study.[7] r_{max} = 3.42 and r_{min} = 0.0 were for UO_2, which was attained from the radial distribution function. The number of defects can be calculated with this method or simply counted by looking at the crystal channels from the ⟨110⟩ direction. However, as the number of defects increases, the defect locations will deteriorate, and it will become increasingly difficult to count visually.

As mentioned above, and clearly seen in Figure 3, two different slopes were acquired above and below the break point for both methods. In our previous study,[8] it was revealed that the most crucial reason for the formation of the linear equation with a steeper slope above the break point than below was the presence of oxygen ions trying to penetrate the octahedrons around the OT uranium defects. Another point in this study, the data obtained by both methods displayed the same gradient below the break point, but they are different above it. Because the DC method creates much more defects (especially oxygen) in the crystal than the MDC method. It was reported that oxygens have an immense effect on structure, volume, and durability of octahedrons.[8] That is, oxygens tend to disrupt octahedrons around the defect. In addition, the values found by the DC method ended (~0.62%) below the saturation point (0.76%–0.81%). This is because there is no linearity in the data obtained above ~0.62%, so it was removed from the figure (Figure 3). The breakpoint was observed to be at the same point in both methods.

Other oxides

Simulations were also carried out using other oxides: CmO_2, AmO_2, CeO_2, NpO_2, PuO_2, ThO_2. A two-part linear equation was observed for each of these molecules with both methods (MDC and DC) (see Supplementary Material-2). Linear equations were fitted to each (first and second) part of the data for both methods, aggregate graphs were created (Figures 4 and 5), and slopes are tabulated in Table 2. Thus, this intriguing result, which applied to uranium dioxide, had also been achieved in other fluorite-type actinide and lanthanide dioxides. The linear values found by the DC method for these molecules ended below the saturation point. Linearity is lost at high doses, so the nonlinear parts removed from the graph (Figure 5 and Supplementary Material-2). The r_{max} and r_{min} data were tabulated in the supplementary material (see Supplementary Material-2).

Table 2 presents Δv_F volume increments per OT cation defects, which was attained from primary and secondary slopes. The equation for volume increment is given as follows,[1,3]

$$\frac{\Delta V}{V} = \frac{3\Delta a}{a_0} = \rho_D \Delta v_F. \quad (1)$$

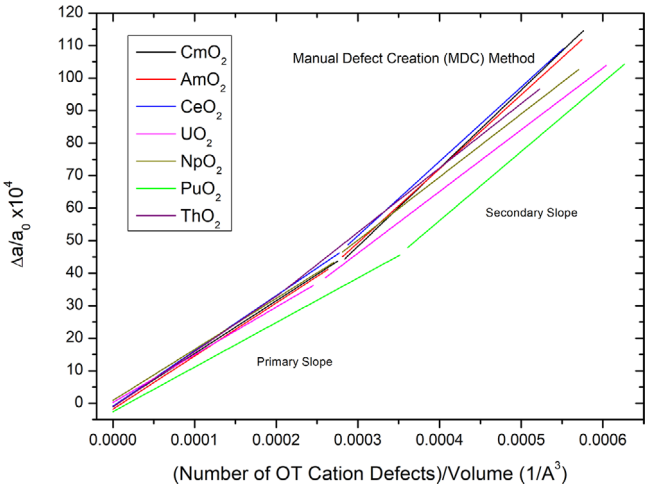


FIGURE 4 The lattice parameter changes of oxides versus the obstruction type (OT) cation defect concentration using manual defect creation (MDC) method. Linear curve fitting data were plotted. The original data are in Figure 3 and the supplementary file (see Supplementary Material-2).

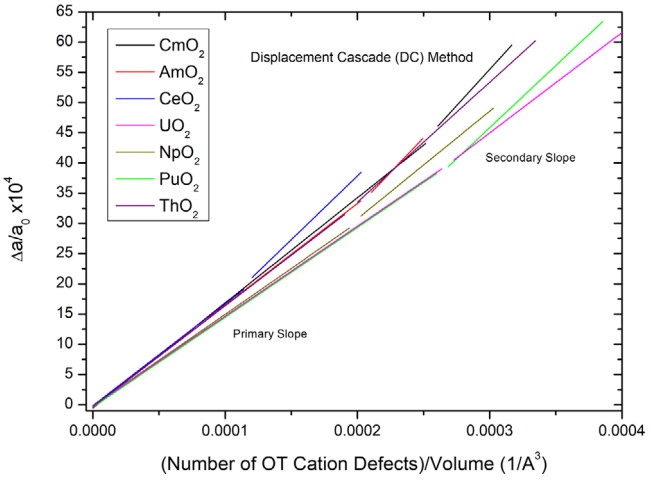


FIGURE 5 The lattice parameter changes of oxides versus the obstruction type (OT) cation defect concentration using displacement cascade (DC) method. Linear curve fitting data were plotted. The original data are in Figure 3 and the supplementary file (see Supplementary Material-2).

The equation is the first-order approximation of a general equation and is only valid for cubic structures.[1] $(\Delta a/a_o \times 10^4)/\rho_D$ is the slope of the fractional change of lattice parameter versus OT cation defect concentration (see Figure 3 and Supplementary Material-2). a_0 is the perfect lattice parameter. $\rho_D = N_{OT}/V$ is the defect concentration. Here, N_{OT} is the OT cation defect number in the supercell, V is the defected cell volume. Although there were many defects in the irradiated lattice, only OT cation defects were taken into account in determining volumetric increases. The use of the equation differs from previous

15512916, 2023, 6, Downloaded from https://ceramics.onlinelibrary.wiley.com/doi/10.1111/jace.19020 by Yildiz Teknik University, Wiley Online Library on [10/07/2025]. See the Terms and Conditions (https://onlinelibrary.wiley.com/terms-and-conditions) on Wiley Online Library for rules of use; OA articles are governed by the applicable Creative Commons License

TABLE 2 The third and fourth columns were slopes of lattice parameter changes with obstruction type (OT) cation defect concentration. The fifth and sixth columns were volume increments per OT cation defects. The last column was the difference between the sixth and fifth columns. Both manual defect creation (MDC) and displacement cascade (DC) methods were shown in the table. The molecules in the table were ordered from top to bottom according to their cation ionic radii (+4) (small to large).

Method	Molecule	Primary Slope	Secondary Slope	Primary $\Delta v_{F1}(Å^3)$	Secondary $\Delta v_{F2}(Å^3)$	Difference $\Delta v_{F2} - \Delta v_{F1}$
MDC	**CmO_2**	162059	240300	48.6177	72.09	23.4723
	AmO_2	163188	227526	48.9564	68.2578	19.3014
	PuO_2	137004	212349	41.1012	63.7047	22.6035
	CeO_2	169861	228586	50.9583	68.5758	17.6175
	NpO_2	156905	193971	47.0715	58.1913	11.1198
	UO_2	146613	189774	43.9839	56.9322	12.9483
	ThO_2	170453	197927	51.1359	59.3781	8.2422
DC	**CmO_2**	173990	239960	52.197	71.988	19.791
	AmO_2	168477	229453	50.5431	68.8359	18.2928
	PuO_2	148806	205778	44.6418	61.7334	17.0916
	CeO_2	168705	211163	50.6115	63.3489	12.7374
	NpO_2	151775	178044	45.5325	53.4132	7.8807
	UO_2	148784	166047	44.6352	49.8141	5.1789
	ThO_2	167163	198596	50.1489	59.5788	9.4299

works[1,3] in this respect, when using the same equation only OT defect is taken into account, but not all defects. Therefore, it will not make sense to compare the results, Δv_F, of this study with the experimental results (see Supplementary Material-3) due to differences in the definition of expression.

In our previous study,[7] $\Delta v_F1 = 46.62Å^3$ and $\Delta v_F2 = 64.97Å^3$ were acquired from the primary and secondary slopes of UO_2 with the MDC method. Former results are compatible with this work for UO_2 (Table 2). A significant relationship between the differences $\Delta v_{F2} - \Delta v_{F1}$ and the effective ionic radii (+4) of cations is revealed by the calculations made with MDC and DC methods. As the radius increases, the differences decrease (Table 2). Statistically, there is an inverse (negative) correlation (see Supplementary Material-3). This situation is plausible: OT cation defects have an octahedral structure around them, and the slope of the linear equation increases in the second part compared to the first part with the penetration of oxygens in these structures. (The effects of oxygen defects on the octahedral structure had been shown in our previous study.[8]) The small ionic radii of the cations result in more oxygens entering/distorting this structure, and consequently, the octahedrons become wider than their original state. That is, there is more available space in the octahedron structure. The difference between two slopes formed by the octahedron structure with and without oxygen increases more for small radius cations. In short, octahedrons around small radius cations expand more than their original states. Namely, a decrease in the radius leads to an increase in the difference.

Finally, the difference between the slopes of first and second parts of the function for ThO_2 is very small in Table 2. Therefore, the graph of ThO_2 (see Supplementary Material-2) could be expressed with a single linear equation. This may mean that there is not enough room to contain oxygen (or less affected by the presence of oxygen) in the octahedron structure around the OT Th defect, which makes it the most stable octahedron at both the low and the high radiation doses/energies compared to other oxides.

3.1.4 | Break, terminal, and maximum points

The lowest possible energy was transferred to the system by applying the MDC method. Defects were placed manually, and energy minimization was performed at the beginning of the simulation. The results obtained by this method could be defined as the condition where the crystal was least exposed to external stress and energy. It could be interpreted as "the ideal" or "the extreme" case in which the defective (or irradiated) crystal exhibits its maximum capacity. These expressions will be referred further in the discussion section. On the other hand, the crystal was exposed to "realistic" radiation conditions with the DC method by energizing the system via PKA atoms.

According to these explanations, Table 3 can be interpreted as follows: Breakpoints and terminal points, which

15512916, 2023, 6, Downloaded from https://ceramics.onlinelibrary.wiley.com/doi/10.1111/jace.19020 by Yildiz Teknik University, Wiley Online Library on [10/07/2025]. See the Terms and Conditions (https://onlinelibrary.wiley.com/terms-and-conditions) on Wiley Online Library for rules of use; OA articles are governed by the applicable Creative Commons License

TABLE 3 Tabulated data were obtained from lattice parameter changes, y, versus obstruction type (OT) cation defect concentration, x, data for each molecule with both methods (MDC and DC). Minimum values were underlined and maximum values were written in bold.

Method	Molecule	Break Point ($x \times 10^{-4}$, y)	End Point ($x \times 10^{-4}$, y)
MDC	**CmO_2**	(2.77, 0.44%)	(5.76, **1.14%**)
	AmO_2	(2.63, 0.41%)	(5.74, 1.11%)
	CeO_2	(2.78, **0.46%**)	(5.5, 1.08%)
	UO_2	(2.46, 0.36%)	(6.05, 1.04%)
	NpO_2	(2.69, 0.43%)	(5.69, 1.02%)
	PuO_2	(**3.5**, **0.46%**)	(**6.25**, 1.04%)
	ThO_2	(2.04, 0.33 %)	(5.2, 0.96%)
DC	**CmO_2**	(2.53, **0.44%**)	(3.17, 0.59%)
	AmO_2	(2.03, 0.34%)	(2.49, 0.44%)
	CeO_2	(1.16, 0.1 9%)	(2.02, 0.38%)
	UO_2	(**2.64**, 0.39%)	(**4.04**, 0.62%)
	NpO_2	(1.95, 0.29%)	(3.04, 0.49%)
	PuO_2	(2.57, 0.38%)	(3.85, **0.64%**)
	ThO_2	(1.91, 0.32%)	(3.36, 0.60%)

are the points where the first and second linear equation ends, were acquired from lattice parameter changes with OT cation defect concentration data for each of the oxides (see Figure 3 and Supplementary Material-2). The PuO_2 molecule has the highest OT cation defect concentration value at the break and the terminal points among other oxide molecules with the MDC method (Table 3). This implies that when the first and the second linear regions of oxides are examined, it is the molecule with the most "defect-bearing capacity" or "concentration" for both regions. Although the OT defect concentration in the first region maximizes the corresponding lattice as expected (0.46%), the effect in the second region is average (1.04%). The concentration of the ThO_2 molecule is at the lowest level among oxides at the break and the terminal points with the MDC method. The low concentration of Th OT defects and the corresponding amount of expansion in the lattice appear to be consistent. When the DC method is applied, where there are external excitations and energy transfers, the defect-bearing capacity of CeO_2 is at the minimum at the break and terminal points. Namely, external excitations easily affect OT defects and collapse the octahedral structures around them in CeO_2.

OT cation defect concentrations versus "cation IFP" and "PKA number" of oxides were obtained by using MDC and DC methods (Figures 6 and 7), respectively. The adjacent concentration values in the y-axis direction at the saturation point for the MDC method were separated when the DC method was applied. When two methods are compared, the most notable change among saturation points occurred in CeO_2 (5.5×10^{-4} Å^{-3} → 2.02×10^{-4} Å^{-3}). The y-axis data of the entire curves in Figure 6 correspond to the x-axis of Figure 3 and figures in Supplementary Material-2 for the MDC method. The y-axis of the bold part of the curves in Figure 7 corresponds to the x-axis of Figure 3 and figures in Supplementary Material-2 for the DC method. Parts, where there was no linearity, were removed from Figure 3 and figures in Supplementary Material-2 (so in Figure 5 also) for the DC method as mentioned in Section 3.1.3. That is, bold parts (Figure 7) correspond to the linear data. The following normal parts (Figure 7) are the nonlinear data, which are not shown in figures (Figure 3 and Supplementary Material-2) for the DC method. Interestingly, the bold parts (Figure 7) end just before reaching the saturation level for all oxides. The OT cation defect concentration saturation levels determined by both methods led to different rankings. Those obtained from Figure 6 and

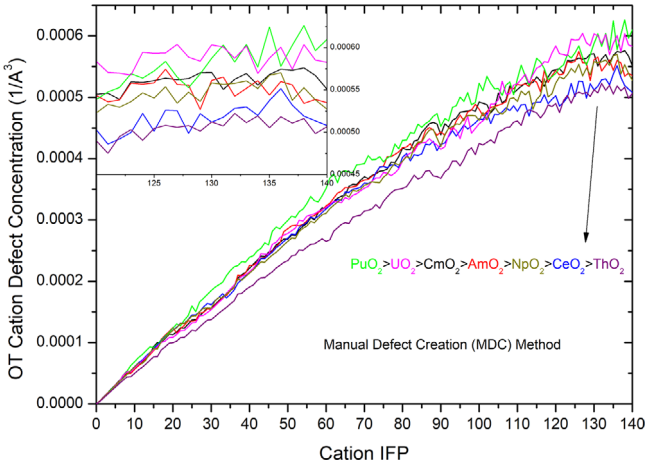


FIGURE 6 Obstruction type (OT) cation defect concentration versus cation IFP data.

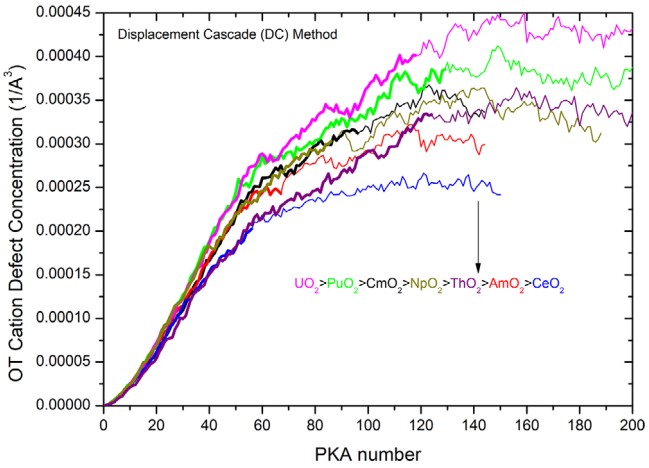


FIGURE 7 Obstruction type (OT) cation defect concentration versus PKA number data.

15512916, 2023, 6, Downloaded from https://ceramics.onlinelibrary.wiley.com/doi/10.1111/jace.19020 by Yildiz Teknik University, Wiley Online Library on [10/07/2025]. See the Terms and Conditions (https://onlinelibrary.wiley.com/terms-and-conditions) on Wiley Online Library for rules of use; OA articles are governed by the applicable Creative Commons License

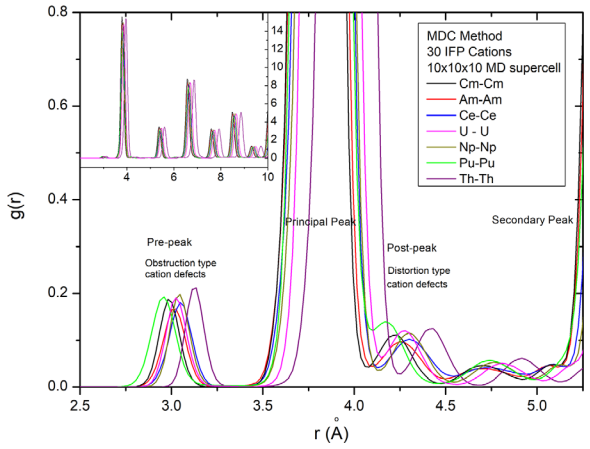


FIGURE 8 Cation-cation radial distribution functions of simulation boxes for "30 IFP cations."

Figure 7 should be examined in more detail, investigated at the microscopic level, and explanations should be provided while transitioning from the MDC to the DC method. The obvious difference between the two methods is the amount of energy transferred to the system. We think that the examinations made by comparing both methods will contain more information than the data obtained with only one method.

Finally, although not the same, in Weber's study,[3] the number of defects per unit cell for polycrystalline structures was calculated (PuO_2, UO_2, CeO_2), and it is consistent with the order obtained from the MDC method and similar to the DC method (see Figure 6, Figure 7 and Supplementary Material-3). The types of defects referred in both studies are not the same, but it is important to mention the experimental study when discussing the OT cation concentration. That is, an increase in the number of OT defects in the lattice leads to an enhancement in the number of other defects.[7,8]

3.2 | Radial distribution functions and visual observations

Figures 8–11 represent cation-cation radial distribution functions (RDFs) with MDC and DC methods. The RDF designates how the density changes as a function of the distance around a central reference atom. The effects of atomic configurations on RDF data were examined by considering two different groups. These groups represent samples from the first (primary slope) and second (secondary slope) regions in linear equations (Figures 4 and 5). They also can be considered as "low" and "high" doses of α-irradiation. 30 IFP cation (Figure 8) samples with the MDC method and 30 PKA number (Figure 9) samples with the DC method are from the first group. 100

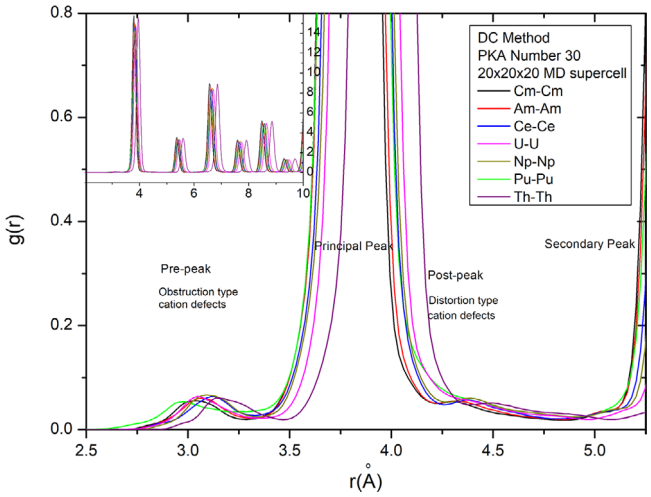


FIGURE 9 Cation-cation radial distribution functions of simulation boxes for "PKA number 30."

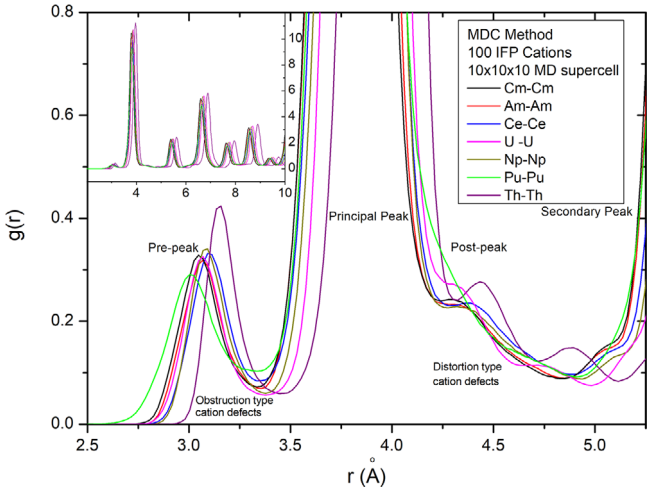


FIGURE 10 Cation-cation radial distribution functions of simulation boxes for "100 IFP cations."

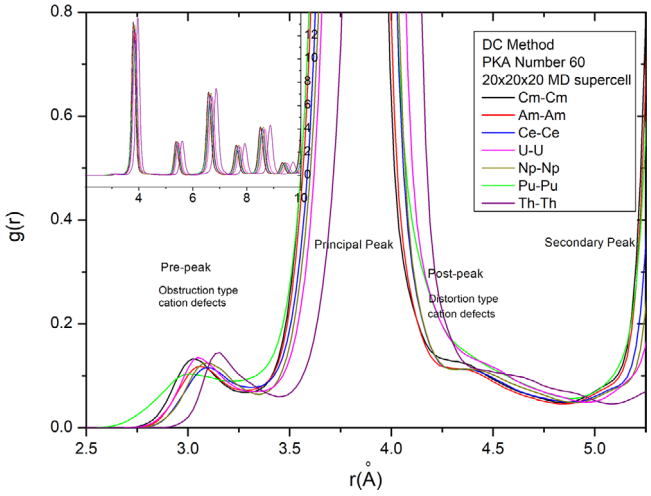


FIGURE 11 Cation-cation radial distribution functions of simulation boxes for "PKA number 60."

15512916, 2023, 6, Downloaded from https://ceramics.onlinelibrary.wiley.com/doi/10.1111/jace.19020 by Yildiz Teknik University, Wiley Online Library on [10/07/2025]. See the Terms and Conditions (https://onlinelibrary.wiley.com/terms-and-conditions) on Wiley Online Library for rules of use; OA articles are governed by the applicable Creative Commons License

IFP cation (Figure 10) samples with the MDC method and 60 PKA number (Figure 11) samples with the DC method are from the second group. The OT defect, DT (distortion type) defect, pre-peak, post-peak, principal peak, secondary peak are essential terms when referring to atoms and RDF data. Pre- and post-peaks that do not exist in perfect crystal structures around principal peaks were observed in all irradiated isostructural oxide RDF graphs. Samples irradiated with both low and high α-particle doses were discussed in pre- and post-peak subsections, below. These peaks were examined from two different perspectives; peak position of a molecule relative to peak positions of other molecules and peak position of a molecule relative to its principal peak position.

3.2.1 | Pre-peaks

Pre-peaks, which do not exist in undamaged crystal structures, have emerged markedly in the range 2.5Å-3.5Å for all oxides in this study (see Figures 8–11). Significant peaks with precise boundaries indicate that atoms are stationary in the crystal and retain their structure. This proves that there is a new interstitial cation defect position (actually a OT defect as described in the introduction part) from a reference cation atom for all isostructural oxides in this study which is closer than the nearest neighbor cation-cation distances (principal peaks in Figures 8–11). All molecules exhibited similar properties under the same dose of irradiation. The projection of the highest point of the pre-peak on the x-axis is the most likely location where the defect is located. The pre-peak heights ($g(r) \approx 0.1 - 0.4$) are small compared to both principal peak levels ($g(r) \approx 11 - 15$) and the average cation density level ($g\,(r) = 1$) in the RDF graph. These values also give us information about the probability of the defect being found at that point or the concentration in the crystal.

A similar peak was observed in our previous studies[7,8] for uranium dioxide, and it was proved that the OT uranium defect was trapped in an octahedral cage, which was coordinated with six other uranium ions. These defects can easily be detected by visual observations of crystal structures from the ⟨110⟩ direction. The instantaneous OT defect position and closest cation distances for the UO_2 molecule (Figures 12A and 13A) corresponding to the U-U pre-peak positions of samples from MDC and DC methods (Figures 8 and 9), respectively, performed in this study were visually consistent. Analogously OT cation defects exist in all other oxide molecules investigated in this study, and they were surrounded by six other cations. Snapshots of these molecules and defect-free UO_2 are in the supplementary material (Supplementary Material-4). Six cations surrounding the OT defect will also be referred to as DT defects in the following section.

All pre-peaks have clear and definite boundaries in radial distribution function with the MDC method (Figure 8). Therefore, the number of defects can be calculated precisely without dispersion in data. Although the uncertainty for the upper limits of the pre-peaks on the x-axis in Figure 10 has increased, the boundaries are still evident for the MDC method. In Figures 9 and 11, pre-peaks have broad and less prominent boundaries with the DC method. The lack of clarity of pre-peak boundaries increases uncertainty in calculations and makes it challenging to determine the number of OT defects $\overline{M_\alpha}$ because it is crucial to set an upper and a lower limit (see Supplementary Material-2) on the x-axis for the equation.[7] Despite all this, the defect concentrations obtained by MDC and DC methods were close to each other at low and high doses of alpha-particle radiation.

Although all oxides investigated in this study generally exhibit similar behavior in the RDF graph, PuO_2, and ThO_2 molecules differ slightly from others. The ThO_2 pre-peak is somewhat higher and shifted to the right (~3.12Å with MDC [Figure 8], ~3.15Å with DC [Figure 9]), and the PuO_2 pre-peak is somewhat lower and shifted to the left (~2.96Å with MDC [Figure 8], ~2.98Å with DC [Figure 9]) than others. The average positions of the other molecular peaks are ~3Å and ~3.04Å for MDC and DC methods, respectively, for low doses of α- irradiation (Figures 8 and 9). As in low doses of α-irradiated samples (Figures 8 and 9), the RDF pre-peaks of high doses of α-irradiated samples (Figures 10 and 11) for PuO_2 (~3Å for MDC and DC) and ThO_2 (~3.15 Å for MDC and DC) are located on the left- and right-hand sides of other pre-peaks (~3.07Å for MDC and DC), respectively. The ThO_2 molecule has a steeper pre-peak with more evident boundaries. The PuO_2 pre-peak has more indistinct borders and a flattened shape, compared to others. Thus, the number of defects for ThO_2 can be calculated more precisely with less uncertainty than other molecules with both methods.

3.2.2 | Post-peaks

The emergence of post-peaks in Figures 8–11 indicates DT (distortion type) cation defects. The main reason for the occurrence of these defects is OT cation defects. Aligned cations in their normal positions are disturbed due to the presence of OT cation defects. OT cation defects are surrounded by an octahedral cage with six cations at its corners (Figures 12B and 13B and see Supplementary Material-4). These six cations in their normal positions are pushed diagonally (four cations on the horizontal plane)

15512916, 2023, 6, Downloaded from https://ceramics.onlinelibrary.wiley.com/doi/10.1111/jace.19020 by Yildiz Teknik University, Wiley Online Library on [10/07/2025]. See the Terms and Conditions (https://onlinelibrary.wiley.com/terms-and-conditions) on Wiley Online Library for rules of use; OA articles are governed by the applicable Creative Commons License

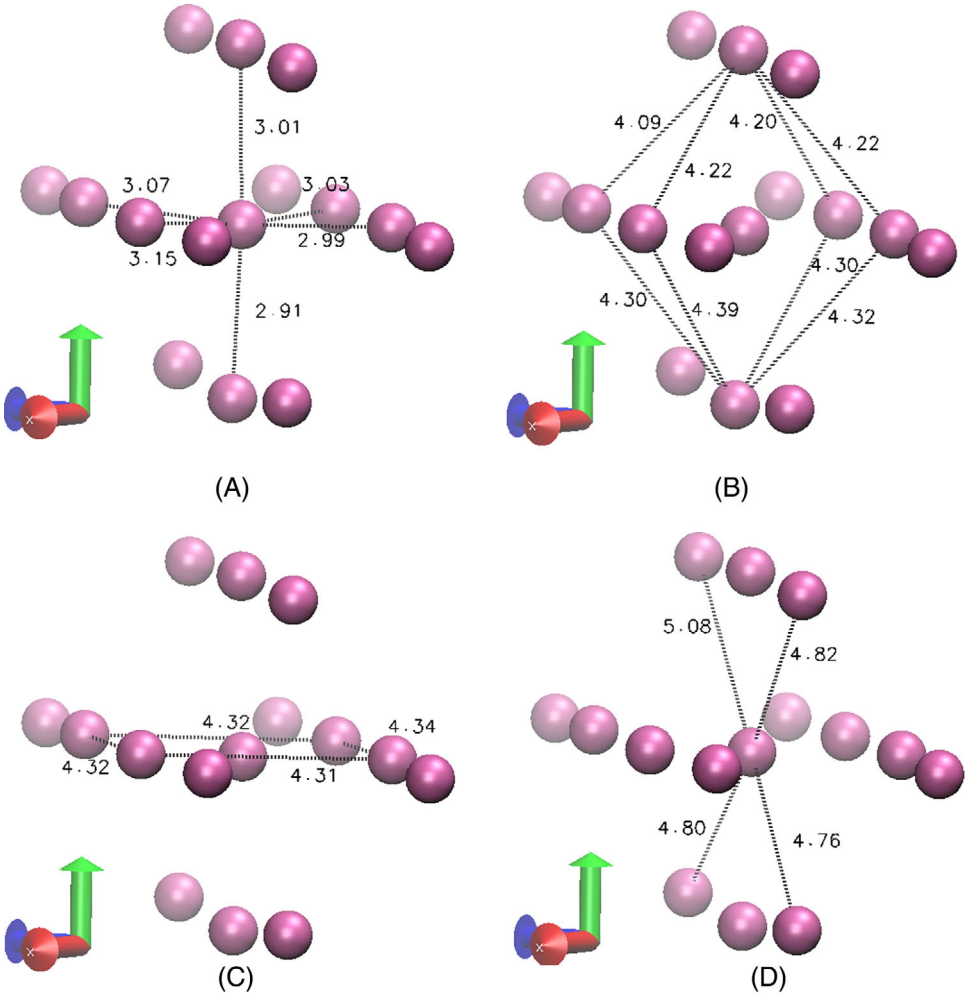


FIGURE 12 Obstruction type (OT) uranium defect was visualized from the ⟨110⟩ direction in "30 IFP cation" sample, which was obtained by manual defect creation (MDC) method. Interatomic distances were indicated. The figure was slightly tilted about the y-axis (green arrow), and oxygen atoms were removed from the figure for reasons of better viewing and clarity. The four snapshots in A, B, C, and D are identical.

and perpendicularly (two cations on the vertical axis) into the ⟨110⟩ channel due to the OT cation defect, which is called the DT defect. These forces are in the directions indicated by dashes (Figures 12A and 13A and see Supplementary Material-4). Irregularities in the alignment of cations can be noticed by visual observations from ⟨110⟩ direction (see Supplementary Material-5). DT defects were driven out of their normal positions. Their effects can also be observed in RDFs with the emergence of new peaks (post-peaks) between 4Å–4.55Å (Figures 8–11), which is consistent with instantaneous interatomic distance values between DT cation-DT cation defects (Figures 12B,C and 13B,C and see Supplementary Material-4). The side lengths (DT cation-DT cation distances) of a random octahedron at a low alpha-radiation dose were examined (see Supplementary Material-5). Linear equations were fitted to each of the eight interatomic distance data over time (20 ps-100 ps). In this particular sample, the average values of linear equations are between 4.26Å–4.36Å. They differ slightly from each other, that is, the octahedron has a minor asymmetric structure on average.

Despite the emergence of pre- and post-peaks (Figure 8), and change in all other parts of RDF data (inset in Figure 8), 30 IFP sample data resemble the crystal structure. This will change with increasing α-irradiation doses and acquire an amorphous-like appearance. Post-peaks with evident boundaries are seen in RDF graphs for each of the 30 IFP oxide samples in the range of 4Å–4.55Å, which corresponds to low α-irradiation doses. Noticeable peaks in Figure 8 indicate the uniform and isolated distribution of distortion type defect positions. The post-peak of PuO_2 is adjacent to its principal peak. Post-peaks of other oxides are relatively distant from their principal peaks when compared with PuO_2. It can be concluded that the DT defects of other oxide molecules hinder the ⟨110⟩ channel more than DT defects of PuO_2. Post-peaks of PuO_2 and ThO_2 are

15512916, 2023, 6, Downloaded from https://ceramics.onlinelibrary.wiley.com/doi/10.1111/jace.19020 by Yildiz Teknik University, Wiley Online Library on [10/07/2025]. See the Terms and Conditions (https://onlinelibrary.wiley.com/terms-and-conditions) on Wiley Online Library for rules of use; OA articles are governed by the applicable Creative Commons License

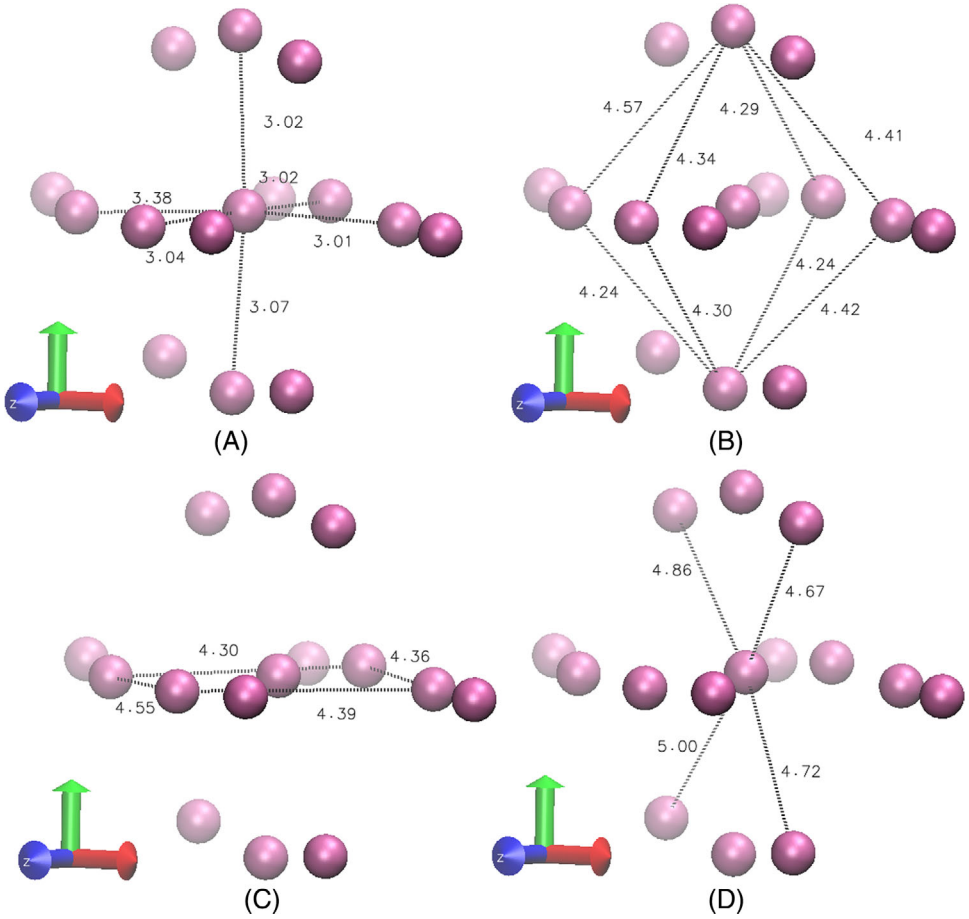


FIGURE 13 Obstruction type (OT) uranium defect was visualized from the ⟨110⟩ direction in "30 PKA number" sample, which was obtained by displacement cascade (DC) method. Interatomic distances were indicated. The figure was slightly tilted about the y-axis (green arrow), and oxygen atoms were removed from the figure for reasons of better viewing and clarity. The four snapshots in A, B, C, and D are identical.

located to the right and left of the average position of other oxide molecules post-peaks (Figure 8).

Distortion type defects for 100 IFP samples (Figure 10), which correspond to high α-radiation doses, resemble atoms that are exposed to high temperatures due to their misalignment. RDF graphs show that the cation sub-lattice has an amorphous-like appearance even at room temperature (inset in Figure 10). The most important indicators of this phenomenon, when compared to an undamaged crystal, are broadening and decrease in heights of RDF peaks, and the fact that RDF data never descended to the zero level on the y-axis above 2.5Å. It is difficult to find isolated defects at this level of radiation dose.

Isostructural oxides with 100 IFP samples can be roughly divided into three groups by analyzing RDF data between 4Å–4.55Å (Figure 10). It is impossible to determine a precise location for DT defects of PuO_2 molecule which belongs to the first group. The probability of finding the DT defect from the edge of the principal peak (~4.2Å) toward 4.55Å is gradually decreasing. In the second group (UO_2, CmO_2, AmO_2, CeO_2, NpO_2), the peaks appear vaguely in the range of 4.2Å–4.55Å. In the third group, ThO_2 post-peak (4.3Å–4.55Å) is clearly visible.

Another post-peak was also observed in the range 4.55Å–5.0Å (Figures 8 and 10). As the visual data are examined, it was determined that these peaks were related to OT cation defect-cation distances (Figure 12D). Therefore, it is more appropriate to call these "pre-peak of secondary peak." OT defect-cation distance values in figure verify RDF data. All these pre-peaks of secondary peaks are visible for 30 IFP samples, whereas only ThO_2 and UO_2 pre-peaks emerge in 100 IFP samples for the MDC method. In the calculations made with the DC method at low and high radiation doses, the uncertainties in the post-peaks and pre-peaks of secondary peaks make it challenging to interpret figures (Figures 9 and 11) and impossible to find the locations of corresponding atomic positions (Figure 13B–D), but the results achieved from the MDC method provide us clues.

15512916, 2023, 6, Downloaded from https://ceramics.onlinelibrary.wiley.com/doi/10.1111/jace.19020 by Yildiz Teknik University, Wiley Online Library on [10/07/2025]. See the Terms and Conditions (https://onlinelibrary.wiley.com/terms-and-conditions) on Wiley Online Library for rules of use; OA articles are governed by the applicable Creative Commons License

4 | DISCUSSION

In our previous study,[7] the dependence of the change in α-particle irradiated UO_2 lattice parameter with the number of OT uranium defects was examined, and it was shown that there was a linear relationship between them. It was also observed that this linear dependence consists of two parts with different inclinations. In the present study, this dependency was tested by increasing the number of atoms in the MD simulation box, implementing another interaction potential (EAM[23,25]) instead of Yakub's potential,[26,27] using LAMMPS[24] program instead of MOLDY,[28] and deploying a more realistic irradiation method (DC) besides the previous one (MDC). Additionally, some calculations were re-performed with Yakub's pair potential, and the results were compared with the data of EAM potential (see Supplementary Material-6). Despite all these changes, the results obtained previously did not change and two-part linearity still exists. Another critical question in this study was whether there was a similar incident in some other fluorite-structured actinide and lanthanide dioxides (CmO_2, AmO_2, CeO_2, NpO_2, PuO_2, ThO_2). It was interesting to find the presence of this phenomenon in these molecules. This means that a general statement could be suggested about these oxides. A general definition for all fluorite-structured dioxides or other fluorite-structured molecules can currently be speculative, and further research is needed. Finally, a loss of linearity was observed at high doses of α-particle radiations below the saturation point while modeling with the DC method.

The dependence of some single- and poly-crystal fluorite-type oxide lattice dilation on α-particle irradiation doses displayed exponential increases in experiments.[1,3] Similarly, the expansion of single-crystal oxide lattices with respect to cation IFP and PKA number investigated by the MD method in this study demonstrates exponential dependencies. Saturation points of these data obtained from experiments and MD simulations were compared. Structures of interest in this study are single-crystal oxides, however, materials used in experiments are generally polycrystalline oxides except for few studies with UO_2.[1,5] Despite this, a similarity detected between single-crystal MD simulation and polycrystalline experimental data. When the saturation levels of single-crystal materials calculated from the simulation were sorted, it was noticed that saturation levels of α-particle irradiated polycrystalline oxides obtained in experiments were compatible with this order (Table 1). However, the results found have no relation to polycrystalline oxides subjected to the α-decay event (Table 1). This is not surprising considering that even the experimental results of different groups for the same material were not consistent with each other (Table 1). One of the main reasons for this is thermal spikes caused by recoil atoms during the α-decay. The rapid increase in temperature can cause the annihilation of some part of OT cation defects randomly, which is called the annealing probability of OT defects. The sensitivity to conditions of material preparation is the other reason.

It was known that the saturation point of relative lattice increase for UO_2 obtained from the α-decay (0.4%−0.5%) was at a different level from the α-particle radiation (0.84%) (Table 1). The upper point of the first region of the linear equation (break point) (0.36%−0.5%) (see Supplementary Material-1 and Table 3) is decisive for the saturation point of the α-decay event. α-decay destroys the second region, but the first region is not affected. Moreover, both the first and the second regions vanished due to fission radiation (~0.1%).[4,8] Regions collapse as the radiation type changes and the energy of the PKA increases. Besides, the lower and upper limits of PKA energies for each radiation type could be determined using the DC method (see Supplementary Material-1).

Another result obtained in this study is that as a result of the calculations made with the DC method, it was observed that there is an upper limit in the expansion data of the lattices (0.82%−0.84%). Above this limit, the fluorite structure collapses regardless of the molecule type (Figure 2). When this limit is exceeded, the simulation axes show very large and abrupt changes relative to each other. It is necessary to examine whether this situation is an artificial, simulation-specific situation or is related to a real physical event. This point is particularly emphasized because Weber stated that the saturation point was 0.84% in his experiment, but he found this value using the curved fit method. In fact, the experimental data ended at ~0.8%.[2] It was not explained in his studies why experiments were not advanced to the saturation point.

The volume increments per OT cation defect, Δv_F, were calculated from the first and second parts of the linear curves. The differences between two data were found, and it was shown that they were inversely proportional to the ionic radii (+4). That is, the gap between the two regimes (first and second parts) is large for small ionic radius cations in octahedral structures. So, the effects of oxygen defects on the octahedron structure vary according to the ionic radius of the OT cation defect. Small radius OT cations would have more free space around them and oxygens can affect them more easily.

OT cation defects are located at octahedral sites surrounded by six other cations. These octahedrons do not have perfect shapes and have slight asymmetries. This minor asymmetry is likely to increase at high radiation doses. The shape and the distribution of the asymmetric

15512916, 2023, 6, Downloaded from https://ceramics.onlinelibrary.wiley.com/doi/10.1111/jace.19020 by Yildiz Teknik University, Wiley Online Library on [10/07/2025]. See the Terms and Conditions (https://onlinelibrary.wiley.com/terms-and-conditions) on Wiley Online Library for rules of use; OA articles are governed by the applicable Creative Commons License

octahedron structure had not been studied in detail here. The change of these structures depending on temperature and radiation should be investigated. The forces acting on the octahedron surfaces could be measured. As these structures have a direct impact on the lattice dilation, this part requires further investigation. Possible reasons for the asymmetry can be real-physical and/or simulation-dependent situations. Physically, the presence of oxygens in the environment may cause this. The direction in which the OT cation defect repels other cations can be significant. The distribution of defects can also be an influencing factor. The simulation-dependent situation for this asymmetry may be the exposure of MD simulation boxes to the NPT ensemble that allows the supercell box axes to change independently. In future studies, octahedron cage structures could be examined by applying hydrostatic pressure to MD boxes, but we think that it would be more accurate for the axes to be independent of each other during the simulation.

Two types of methods were used to simulate the irradiated crystal structures. These were utilized to make comparisons/verifications with each other and experiment. DC method is a more realistic method compared to MDC. However, the MDC method is essential in terms of displaying "the maximum capacity" of the crystal. The maximum point the crystal can swell or the maximum number of defects it can contain are some examples for this expresion. It is a useful method to interfere with the crystal with very little external stimuli (energy, temperature) and to measure physical data in such an extreme case. In the future, such an environment can also be established experimentally, and these limit conditions may have practical consequences.

5 | CONCLUSION

Imperfections and temperature have a direct effect on the change of lattice constant of an irradiated molecule. The swelling of the lattice was determined as a result of the delicate balance between defect concentration and temperature (e.g., thermal spikes). In this study, the effects of OT-type cation defects on some actinide and lanthanide dioxides with the fluorite-type structure were discussed, and their importance was revealed. As a result of these findings, linear relationships between OT cation defect concentrations versus lattice dilatation were shown for all oxides in this study. It had been shown that all linear equations of oxides consist of two regions. With these results, it is now clear why there are different levels of lattice saturation points for different radiation types (α-particle, α-decay, fission). As a by-product of this study, it has been shown that the energy range of PKAs formed by a radiation type can be determined by using the DC method as described in the article. Finally, the adequacy of the MDC method was demonstrated when compared with the DC and FPA methods.

For future studies, computer tests involving other defects (e.g., clusters, radiogenic Pb, He, etc.) should be performed to inspect the extent of the defect effects besides the perfect crystal. Studies should also be made on polycrystalline actinide and lanthanide dioxides, and the effects of OT defects on these structures should be investigated. The relationship between OT defects with other physical quantities, like thermal conductivity, diffusion, ionic conductivity, heat capacity, electronic properties, etc., should also be studied so that some events that have not been fully explained so far can be solved, or a new perspective can be provided for the already described events. For example, the variation of OT defects in the crystal directly affects the lattice constant and abrupt changes in the lattice parameter were observed in the recovery of each OT defect.[8] Similar effects may occur on the above-listed physical properties, and these discrete/intermittent changes may lead to technological applications. Research should be extended by adding the effect of temperature to all these studies. The study should be further expanded, and a more general theory should be put forward by studying all fluorite-structured oxides or other fluorite-structured molecules.

ACKNOWLEDGMENTS

The numerical calculations reported in this paper were partially performed at TUBITAK ULAKBIM, High Performance and Grid Computing Center (TRUBA resources). Computing resources used in this work were partially provided by the National Center for High Performance Computing of Turkey (UHeM) under grant number: 5003802015.

ORCID

Seçkin D. Günay https://orcid.org/0000-0003-0507-0166

REFERENCES

1. Weber WJ. Ingrowth of lattice defects in alpha irradiated UO_2 single crystals. J Nucl Mater. 1981;98:206–15. https://doi.org/10.1016/0022-3115(81)90400-1
2. Weber WJ. Thermal recovery of lattice defects in alpha-irradiated UO_2 crystals. J Nucl Mater. 1983;114:213–21. https://doi.org/10.1016/0022-3115(83)90259-3
3. Weber WJ. Alpha-irradiation damage in CeO_2, UO_2 and PuO_2. Radiat Eff. 1984;83:145–56. https://doi.org/10.1080/00337578408215798
4. Hj M. Radiation damage in crystalline insulators, oxides and ceramic nuclear fuels. Radiat Eff. 1982;64:3–33. https://doi.org/10.1080/00337578208222984

15512916, 2023, 6, Downloaded from https://ceramics.onlinelibrary.wiley.com/doi/10.1111/jace.19020 by Yildiz Teknik University, Wiley Online Library on [10/07/2025]. See the Terms and Conditions (https://onlinelibrary.wiley.com/terms-and-conditions) on Wiley Online Library for rules of use; OA articles are governed by the applicable Creative Commons License

5. Debelle A, Boulle A, Garrido F, Thomé L. Strain and stress build-up in He-implanted UO_2 single crystals: an X-ray diffraction study. J Mater Sci. 2011;46(13):4683–9. https://doi.org/10.1007/s10853-011-5375-1
6. Chartier A, Onofri C, Van Brutzel L, Sabathier C, Dorosh O, Jagielski J. Early stages of irradiation induced dislocations in Urania. Appl Phys Lett. 2016;109(18):181902. https://doi.org/10.1063/1.4967191
7. Günay SD. Swelling mechanisms of UO_2 lattices with defect ingrowths. PLoS One. 2015;10:e0134500. https://doi.org/10.1371/journal.pone.0134500
8. Günay SD. Thermal recovery mechanisms of UO_2 lattices by defect annihilation. J Alloys Comp. 2017;724:841–50. https://doi.org/10.1016/j.jallcom.2017.07.100
9. Turcotte RP. Alpha radiation damage in the actinide dioxides. Richland, Wash.(USA): Battelle Pacific Northwest Labs; 1975.
10. Mosley WC. Self-radiation damage in curium-244 oxide and aluminate. J Am Ceram Soc. 1971;54(10):475–9. https://doi.org/10.1111/j.1151-2916.1971.tb12182.x
11. Noé M, Fuger J. Self-radiation effects on the lattice parameter of $^{244}CmO_2$. Inorg Nucl Chem Lett. 1971;7(5):421–30. https://doi.org/10.1016/0020-1650(71)80177-0
12. Mendelssohn K, King E, Lee JA, Rand MH, Griffin CS, Street RS. Plutonium 1965. London: Chapman and Hall; 1967.
13. Hurtgen C, Fuger J. Self-irradiation effects in americium oxides. Inorg Nucl Chem Lett. 1977;13:179. https://doi.org/10.1016/0020-1650(77)80091-3
14. Chikalla TD, Eyring L. Phase relationships in the americium-oxygen system. J Inorg Nucl Chem. 1968;30(1):133–45. https://doi.org/10.1016/0022-1902(68)80072-7
15. Keller C. The chemistry of the transuranium elements. Weinheim: Verlag Chemie GmbH; 1971.
16. Noé M, Fuger J. Self-radiation effects on the lattice parameter of $^{238}PuO_2$. Inorg Nucl Chem Lett. 1974;10:7–19. https://doi.org/10.1016/0020-1650(74)80211-4
17. Rand MH, Fox AC, Street RS. Radiation self-damage in plutonium compounds. Nature. 1962;195:567–8. https://doi.org/10.1038/195567a0
18. Schmidt HE, Richter J, Matzke H, van Geel J. The effect of self-irradiation on the thermal conductivity of plutonium and americium oxides. In: Tong TW, editor. Proceedings of the 22nd international conference on thermal conductivity. Lancaster, Penn. : Technomic Pub. Co.; 1994. p. 920–5.
19. Chikalla TD, Turcotte RP. Self-radiation damage ingrowth in $^{238}PuO_2$. Radiat Eff. 1973;19(2):93–8. https://doi.org/10.1080/00337577308232225
20. Debelle A, Crocombette JP, Boulle A, Chartier S, Jourdan T, Pellegrino S, et al. Lattice strain in irradiated materials unveils a prevalent defect evolution mechanism. Phys Rev Materials. 2018;2(1):013604. https://doi.org/10.1103/PhysRevMaterials.2.013604
21. Evron R, Kimmel G, Eyal Y. Thermal recovery of self-radiation damage in uraninite and thorianite. J Nucl Mater. 1994;217:54. https://doi.org/10.1016/0022-3115(94)90304-2
22. Kato M, Komeno A, Uno H, Sugata H, Nakae N, Konashi K, et al. Self-radiation damage in plutonium and uranium mixed dioxide. J Nucl Mater. 2009;393(1):134–40. https://doi.org/10.1016/j.jnucmat.2009.05.020
23. Cooper MWD, Rushton MJD, Grimes RW. A many-body potential approach to modelling the thermomechanical properties of actinide oxides. J Phys Condens Matter. 2014;26:105401. https://doi.org/10.1088/0953-8984/26/10/105401
24. Plimpton P. Fast parallel algorithms for short-range molecular dynamics. J Comput Phys. 1995;117:1–19. https://doi.org/10.1006/jcph.1995.1039
25. Cooper MWD, Stanek CR, Turnbull JA, Uberuaga BP, Andersson DA. Simulation of radiation driven fission gas diffusion in UO_2, ThO_2 and PuO_2. J Nucl Mater. 2016;481:125–33. https://doi.org/10.1016/j.jnucmat.2016.09.013
26. Yakub E, Ronchi C, Staicu D. Molecular dynamics simulation of premelting and melting phase transitions in stoichiometric uranium dioxide. J Chem Phys. 2007;127:094508. https://doi.org/10.1063/1.2764484
27. Devanathan R, Yu J, Weber WJ. Energetic recoils in UO_2 simulated using five different potentials. J Chem Phys. 2009;130:174502. https://doi.org/10.1063/1.3125967
28. Refson K. Moldy: a portable molecular dynamics simulation program for serial and parallel computers. Comput Phys Commun. 2000;126:310–29. https://doi.org/10.1016/S0010-4655(99)00496-8

SUPPORTING INFORMATION

Additional supporting information can be found online in the Supporting Information section at the end of this article.

How to cite this article: Günay SD. Actinide and lanthanide dioxide lattice dilatation mechanisms with defect ingrowths. J Am Ceram Soc. 2023;106:3895–3910. https://doi.org/10.1111/jace.19020

15512916, 2023, 6, Downloaded from https://ceramics.onlinelibrary.wiley.com/doi/10.1111/jace.19020 by Yildiz Teknik University, Wiley Online Library on [10/07/2025]. See the Terms and Conditions (https://onlinelibrary.wiley.com/terms-and-conditions) on Wiley Online Library for rules of use; OA articles are governed by the applicable Creative Commons License